

University of Wollongong

Research Online

---

Australian Institute for Innovative Materials -  
Papers

Australian Institute for Innovative Materials

---

2012

## Microscopic role of carbon on MgB<sub>2</sub> wire for critical current density comparable to NbTi

Jung Ho Kim

*University of Wollongong, jhk@uow.edu.au*

Sangjun Oh

*National Fusion Research Institute Republic Korea*

Yoon-Uk Heo

*Pohang University of Science and Technology*

Satoshi Hata

*Kyushu University*

Hiroaki Kumakura

*National Institute for Materials Science, Tsukuba*

*See next page for additional authors*

Follow this and additional works at: <https://ro.uow.edu.au/aiimpapers>

 Part of the [Engineering Commons](#), and the [Physical Sciences and Mathematics Commons](#)

---

### Recommended Citation

Kim, Jung Ho; Oh, Sangjun; Heo, Yoon-Uk; Hata, Satoshi; Kumakura, Hiroaki; Matsumoto, Akiyoshi; Mitsuhashi, Masatoshi; Choi, Seyong; Shimada, Yusuke; Maeda, Minoru; Macmanus-Driscoll, Judith; and Dou, S X., "Microscopic role of carbon on MgB<sub>2</sub> wire for critical current density comparable to NbTi" (2012). *Australian Institute for Innovative Materials - Papers*. 304.  
<https://ro.uow.edu.au/aiimpapers/304>

Research Online is the open access institutional repository for the University of Wollongong. For further information contact the UOW Library: [research-pubs@uow.edu.au](mailto:research-pubs@uow.edu.au)

---

# Microscopic role of carbon on MgB<sub>2</sub> wire for critical current density comparable to NbTi

## Abstract

Increasing dissipation-free supercurrent has been the primary issue for practical application of superconducting wires. For magnesium diboride, MgB<sub>2</sub>, carbon is known to be the most effective dopant to enhance high-field properties. However, the critical role of carbon remains elusive, and also low-field critical current density has not been improved. Here, we have undertaken malic acid doping of MgB<sub>2</sub> and find that the microscopic origin for the enhancement of high-field properties is due to boron vacancies and associated stacking faults, as observed by high-resolution transmission electron microscopy and electron energy loss spectroscopy. The carbon from the malic acid almost uniformly encapsulates boron, preventing boron agglomeration and reducing porosity, as observed by three-dimensional X-ray tomography. The critical current density either exceeds or matches that of niobium titanium at 4.2 K. Our findings provide atomic-level insights, which could pave the way to further enhancement of the critical current density of MgB<sub>2</sub> up to the theoretical limit.

## Keywords

microscopic, wire, critical, current, role, density, carbon, nbt, comparable, mgb2

## Disciplines

Engineering | Physical Sciences and Mathematics

## Publication Details

Kim, J., Oh, S., Heo, Y., Hata, S., Kumakura, H., Matsumoto, A., Mitsuhara, M., Choi, S., Shimada, Y., Maeda, M., Macmanus-Driscoll, J. & Dou, S. Xue. (2012). Microscopic role of carbon on MgB<sub>2</sub> wire for critical current density comparable to NbTi. *NPG Asia Materials*, 4 (e3), 1-7.

## Authors

Jung Ho Kim, Sangjun Oh, Yoon-Uk Heo, Satoshi Hata, Hiroaki Kumakura, Akiyoshi Matsumoto, Masatoshi Mitsuhara, Seyong Choi, Yusuke Shimada, Minoru Maeda, Judith Macmanus-Driscoll, and S X. Dou

## ORIGINAL ARTICLE

# Microscopic role of carbon on MgB<sub>2</sub> wire for critical current density comparable to NbTi

Jung Ho Kim<sup>1,8</sup>, Sangjun Oh<sup>2,8</sup>, Yoon-Uk Heo<sup>3,8</sup>, Satoshi Hata<sup>4</sup>, Hiroaki Kumakura<sup>5</sup>, Akiyoshi Matsumoto<sup>5</sup>, Masatoshi Mitsuhashi<sup>4,8</sup>, Seyong Choi<sup>5,6</sup>, Yusuke Shimada<sup>4</sup>, Minoru Maeda<sup>1,9</sup>, Judith L MacManus-Driscoll<sup>7</sup> and Shi Xue Dou<sup>1</sup>

Increasing dissipation-free supercurrent has been the primary issue for practical application of superconducting wires. For magnesium diboride, MgB<sub>2</sub>, carbon is known to be the most effective dopant to enhance high-field properties. However, the critical role of carbon remains elusive, and also low-field critical current density has not been improved. Here, we have undertaken malic acid doping of MgB<sub>2</sub> and find that the microscopic origin for the enhancement of high-field properties is due to boron vacancies and associated stacking faults, as observed by high-resolution transmission electron microscopy and electron energy loss spectroscopy. The carbon from the malic acid almost uniformly encapsulates boron, preventing boron agglomeration and reducing porosity, as observed by three-dimensional X-ray tomography. The critical current density either exceeds or matches that of niobium titanium at 4.2 K. Our findings provide atomic-level insights, which could pave the way to further enhancement of the critical current density of MgB<sub>2</sub> up to the theoretical limit.

*NPG Asia Materials* (2012) 4, e3; doi:10.1038/am.2012.3; published online 18 January 2012

**Keywords:** carbon role; densification; 3D tomogram; MgB<sub>2</sub>; TEM

## INTRODUCTION

Soaring liquid helium prices have increased the demand for cryogen-free superconducting magnets more than ever. For example, if magnetic resonance imaging magnets can be operated without liquid helium, it will be definitely beneficial. Even though numerous superconducting materials had already been discovered, MgB<sub>2</sub>, which was found to be superconducting in 2001,<sup>1</sup> is considered as the most promising candidate for cryogen-free operation, replacing conventional NbTi technology, due to its low material cost, simple crystalline structure and relatively high transition temperature of ~40 K.<sup>1–4</sup> A decade-long intensive research effort has led to noticeable progress in the development of MgB<sub>2</sub> wire, and its high-field properties are now much better than those of NbTi, for example, thanks to carbon doping.<sup>5,6</sup> On the other hand, at low field (<5 T), where magnetic resonance imaging magnets are operated, the critical current density has not been increased and is even lower than that of NbTi. The reason why the low-field properties were not improved has been studied, and the lack of enhancement has been mostly attributed to porosity.<sup>7,8</sup> The chemical reaction between magnesium

and boron results in about 30% volume reduction, and porosity is known to be difficult to avoid. However, no quantitative analysis has ever been carried out.

When carbon is doped into MgB<sub>2</sub>,<sup>9,10</sup> it is believed that it substitutes for boron, stiffens the optical  $E_{2g}$  phonon mode, which is strongly linked with anisotropic  $\sigma$  bands and, hence, lowers the transition temperature.<sup>11–13</sup> Increased interband scattering between the  $\pi$  and  $\sigma$  bands could also be a cause for the lower transition temperature.<sup>14</sup> Even without any variation in the interband scattering, the intraband scattering by itself can increase the upper critical field far beyond that of Nb<sub>3</sub>Sn, according to a recent two-band dirty-limit theory.<sup>15</sup> It is also argued from resistivity measurements or from lattice strain estimated from X-ray diffraction that the impurity scattering rate is closely related to the upper critical field enhancement by carbon doping.<sup>12,16,17</sup> The microscopic origin of the increased scattering rate due to doping is not yet clear. Microscopic imperfections, such as porosity, grain boundaries, stacking faults, dislocations, secondary phases and so on, also can act as pinning sites. The critical current density is determined by the balance between the Lorentz force and the pinning force.

<sup>1</sup>Institute for Superconducting and Electronic Materials, University of Wollongong, North Wollongong, New South Wales, Australia; <sup>2</sup>Material Research Team, National Fusion Research Institute, Daejeon, Republic of Korea; <sup>3</sup>Research Facility Center, Graduate Institute of Ferrous Technology, Pohang University of Science and Technology, Pohang, Republic of Korea; <sup>4</sup>Interdisciplinary Graduate School of Engineering Sciences, Kyushu University, Fukuoka, Japan; <sup>5</sup>Superconducting Materials Center, National Institute for Materials Science, Tsukuba, Japan; <sup>6</sup>Busan Center, Korea Basic Science Institute, Jangjeon, Geumjeong, Busan, Republic of Korea and <sup>7</sup>Department of Materials Science and Metallurgy, University of Cambridge, Cambridge, UK

Correspondence: Professor H Kumakura, Superconducting Materials Center, National Institute for Materials Science, Tsukuba, Japan.

E-mail: KUMAKURA.Hiroaki@nims.go.jp

or Professor S X Dou, Institute for Superconducting and Electronic Materials, University of Wollongong, North Wollongong, New South Wales, Australia.

E-mail: shi@uow.edu.au

<sup>8</sup>These authors contributed equally to this work.

<sup>9</sup>Current address: Department of Physics, College of Science and Technology, Nihon University, Tokyo, Japan

Received 14 August 2011; revised 2 November 2011; accepted 8 November 2011

## MATERIALS AND METHODS

The wire samples were fabricated as follows: boron powder (99.9%), toluene (C<sub>7</sub>H<sub>8</sub>, 99.5%) and malic acid (C<sub>4</sub>H<sub>6</sub>O<sub>5</sub>, 99%) were mixed in a Spex mill for 10 min, dried out at 150 °C and then processed in a planetary mill with magnesium powder (99%). The composite powder was put into Nb/Monel cladding and drawn until the outer diameter was reduced to 0.834 mm. Both the doped and the un-doped samples were heat treated at 650 °C for 30 min under argon atmosphere. After the heat treatment, samples were ground until bare MgB<sub>2</sub> core appeared and then mounted on a tungsten tip of an Xradia nanoXCT, a 50-nm-resolution X-ray computed tomography scanner. The critical current density was measured by the standard four-probe method. An electric field criterion of 1 μV cm<sup>-1</sup> was used for the determination of the critical current. Microscopic studies were carried out using a JEOL JEM-2500SE, a Cs-corrected STEM equipped with a Gatan 776 EELS (Enfina 1000). High-magnification images were obtained with a JEOL JEM-3000F, a 300 keV high-resolution TEM. This electron microscope also has a Gatan 863 energy filter (GIF Tridium), so that simultaneous EELS analysis was possible. The high-energy synchrotron radiation powder diffraction experiment was carried out at the SPring-8 facility using a large Debye–Scherrer camera equipped with an imaging plate as a highly sensitive X-ray detector. The synchrotron radiation X-ray diffraction data were analyzed by the Rietveld refinement method using the asymmetric pseudo-Voigt function.

## RESULTS AND DISCUSSION

### Sample preparation and the critical current measurements

Among various carbon doping methods, chemical solution processes using carbohydrate, such as malic acid dissolved in toluene, which is adopted in this work, are advantageous in terms of both cost and performance.<sup>17,18</sup> Carbohydrates easily decompose at, or even below 650 °C, the melting temperature of magnesium, which enables low sintering temperature fabrication to suppress grain growth. Smaller grains are related to larger pinning force and higher critical current,<sup>19–22</sup> according to grain boundary pinning models. It is also claimed that more homogeneous mixing is possible than with other doping methods. A ball milling process was adopted to further enhance the uniformity.<sup>23–25</sup> The mixed un-reacted powders were put into a metallic tube and then heat treated. The field dependence of the critical current measured by the standard four-probe method is shown in Figure 1a. Compared with other types of carbon doping, such as SiC doping,<sup>26–29</sup> the malic acid-doped sample studied in this work not only shows increased high-field critical current density, but also increased low-field critical current density, even comparable to that of NbTi, exceeding 10<sup>5</sup> A cm<sup>-2</sup> at 4.2 K and 6 T. At higher temperature, for example at 20 K, the critical current density of SiC-doped samples has been reported to be decreased compared with the un-doped samples, but here, even at 20 K, the critical current density was increased.

### X-ray tomogram analysis on voids

Two important ways to increase critical current density are by the enhancement of the pinning force<sup>30,31</sup> and/or by increasing the cross-sectional area fraction.<sup>7</sup> First, we consider the area fraction. This was investigated by state-of-the-art 50-nm-resolution X-ray tomography, as shown in Figure 2. Both the doped and un-doped wires were ground until the MgB<sub>2</sub> core appeared, and then 1609 sliced X-ray tomograms covering an area of 15 × 15 μm<sup>2</sup> were collected (continuous motion view for each tomogram can be found in Supplementary Movies 1 and 2) using the Zernike phase contrast method along the wire axis (*z* axis in Figures 2a and b) and also along each of the two other orthogonal axes. MgB<sub>2</sub>, and other phases can be identified from the contrast difference. These sliced tomograms were merged into three-dimensional images and color-rendered, so that red and white

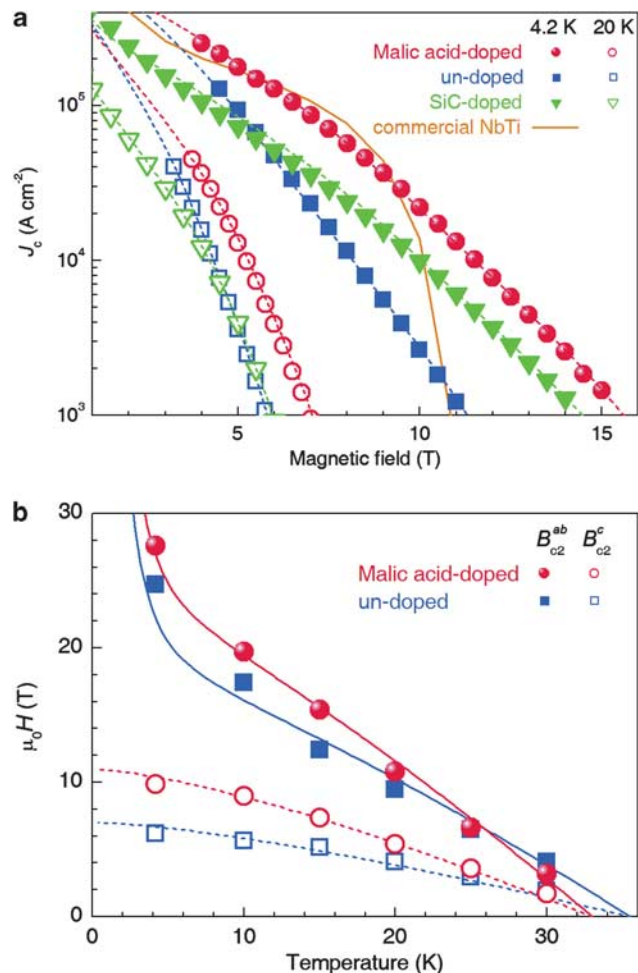


**Figure 1** Field dependence of the critical current density and temperature dependence of the extracted upper critical field. (a) Field dependence of the critical current measured by the standard four-probe method. Dashed lines are calculated from the percolation model. (b) Field dependence of the critical current measured at various temperatures, and the upper critical field extracted at each temperature. Lines are calculated from the two-band dirty-limit theory.

regions correspond to MgB<sub>2</sub> and impurity phases, respectively, as shown in Figures 2a and b. Voids shadowed by MgB<sub>2</sub> or by impurity phases, as shown in Figures 2a and b, can be more clearly identified in the Supplementary Movies (360° rotation along the *z* axis can be found in Supplementary Movies 3 and 4). In the insets of Figures 2a and b, magnified views of the voids are presented. The major difference between the two samples is that for the doped sample, the void size is on average smaller than that of the un-doped sample.

For a quantitative comparison, voids in each sliced tomogram were directly studied using a black and white image contrast method adopted to sharpen the boundary of each void in all the tomograms. Voids were numbered and their physical dimensions, including their area, and major and minor diameters, were measured. The major and minor diameters are defined as the length and width of the void along the longest direction, respectively. The pixel size of each tomogram is 16 nm. Comparative histograms of void area and major or minor diameter along the *z* axis direction are shown in Figures 2c,d,e. To show the difference more clearly, the *y* axes of the histograms are presented as count percentage multiplied by void area, major

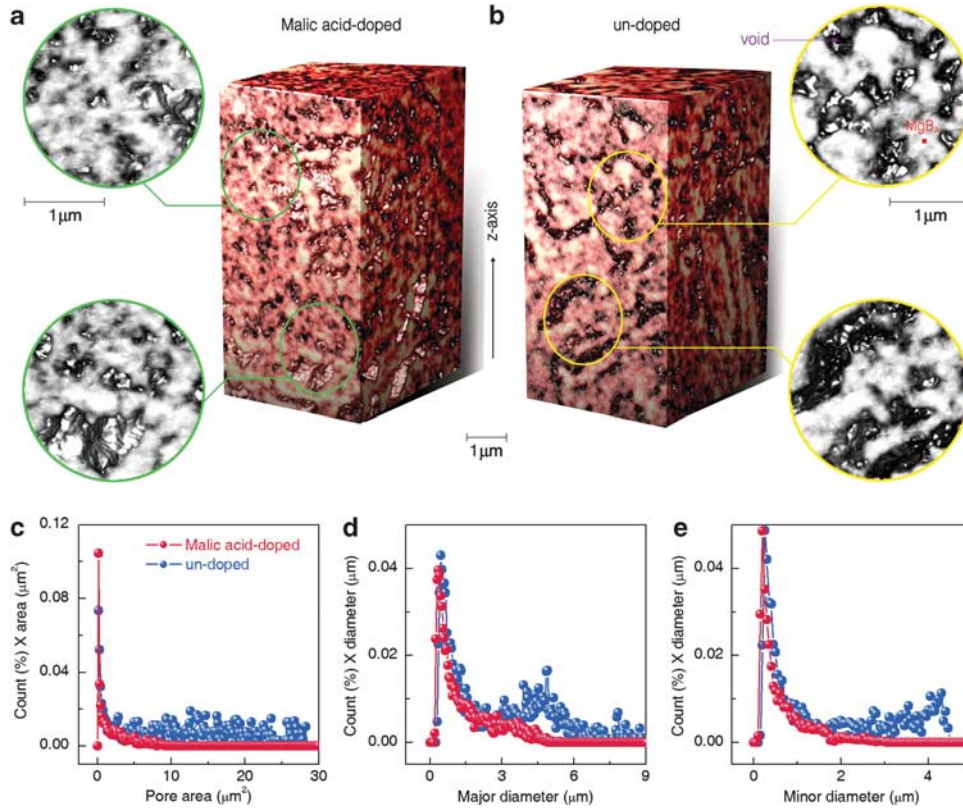


**Figure 2** Cores of powder-in-tube processed MgB<sub>2</sub> wires examined by X-ray tomography. About (15 μm)<sup>3</sup> volume of core region was scanned along each direction for both malic acid-doped and un-doped samples. (a, b) The tomograms along each direction were integrated into three-dimensional images. (c–e) Histograms along the z direction.

**Table 1** List of void physical dimension averages

	Area (μm <sup>2</sup> )	Major diameter (μm)	Minor diameter (μm)	Void fraction (%)	Number of voids
<i>Malic acid doped</i>					
x axis	0.34	0.73	0.37	41.24	17 611
y axis	0.28	0.68	0.34	40.61	21 442
z axis	0.32	0.70	0.32	40.48	18 869
<i>Un-doped</i>					
x axis	1.53	1.23	0.63	50.87	7496
y axis	1.29	1.26	0.64	50.38	8819
z axis	1.41	1.20	0.63	50.33	8009

diameter, or minor diameter, respectively. If there is a preferential direction for voids, the statistical distribution of the voids will be different along each direction. However, we found that the histograms of void area and of major and minor diameters almost coincide with each other for all the directions, especially for the doped sample, which could be attributed to a uniform mixing procedure. The probability distribution of void area is almost same for small-sized voids less than ~2 μm<sup>2</sup>, but there is a noticeable difference in large void distributions. The average void area and the average major and minor diameters along each direction are listed in Table 1.

With malic acid inclusion, the total number of voids is roughly doubled, but the average area is reduced by more than four times. As a result, the void fraction is reduced from around 50% to around 40%, or in other words, the MgB<sub>2</sub> core is densified by doping. Since 1609 sliced X-ray tomograms along each direction were collected with equidistant steps the void fraction is basically an averaged area fraction. Slight discrepancies are due to the finite pixel size in each tomogram, the finite number of tomograms along each direction or the black and white imaging process.

#### The critical current analysis based on the percolation model

Having understood the increase in critical current density as due, at least partly, to the increase in the cross-sectional area fraction, we now consider whether there is a contribution to the enhanced low-field critical current density from increased pinning force. In order to clarify this, the field dependence of the critical current was analyzed by the percolation model,<sup>12,32</sup> where the loss of connectivity caused by voids and the upper critical field anisotropy are considered together. The model has four fitting parameters: the effective pinning force maximum  $F_m^*$ , the upper critical field  $B_{c2}$ , the anisotropy parameter  $\gamma$  and the percolation threshold  $p_c$ . The low-field critical current density is mostly affected by the effective pinning force maximum, which is the pinning force maximum,  $F_m$ , multiplied by area fraction, AF ( $F_m^* = F_m \times AF$ ). The best fit is obtained with the parameters listed in Table 2, and the dashed lines are calculated using those parameters (Figure 1a). For the SiC-doped sample, the effective pinning force maximum was reduced to  $1.84 \times 10^6$  AT cm<sup>-2</sup>, but it is enhanced noticeably by malic acid doping. The enhancement of the effective

**Table 2** Percolation model fitting parameters

	Pinning force maximum (10 <sup>6</sup> ATcm <sup>-2</sup> )	Upper critical field (T)	Anisotropy parameter	Percolation threshold
<i>Malic acid-doped</i>				
4.2 K	4.12	27.6	2.8	0.26
20 K	1.19	10.8	2.0	0.26
<i>Un-doped</i>				
4.2 K	3.77	24.7	4.0	0.26
20 K	1.23	9.45	2.3	0.26
<i>SiC-doped</i>				
4.2 K	1.84	28.0	2.8	0.26
20 K	0.48	9.5	1.85	0.26

pinning force maximum from 3.77 to 4.12×10<sup>6</sup> AT cm<sup>-2</sup> almost exactly matches the reduction in the void fraction from ~50 to ~40%. The pinning force enhancement by doping therefore can be mainly attributed to the increase in the area fraction.

As with other carbon-doped samples, such as SiC-doped samples, the high-field (near the irreversibility field) critical current density is also dramatically increased by malic acid doping, as shown in Figure 1a. From the percolation model analysis, this could be attributed to the enhancement of the upper critical field, or to the reduction in the anisotropy parameters, which are related to the increased impurity scattering rate. The temperature dependence of the upper critical field along the *c* axis and the *ab* plane are shown in Figure 1b. Usually, the upper critical field is determined from the onset of resistive broadening. However, in polycrystalline samples, this might give an underestimation.<sup>29</sup> Instead, the extracted upper critical field and other fitting parameters of the percolation model can reproduce the resistive broadening well. The relevance of the extracted upper critical field to the actual value was also reported in the early work of Eisterer *et al.*<sup>32</sup> From the field dependence of the critical current (Figure 1a) at each temperature, the upper critical field was extracted using the percolation model. The extracted upper critical field shown in Figure 1b was fitted by the following two-band dirty-limit theory,<sup>15</sup>

$$2w[\ln t+u(b/t)][\ln t+u(\eta b/t)]+\lambda_2[\ln t+u(\eta b/t)] + \lambda_1[\ln t+u(\eta b/t)] = 0 \quad (1)$$

where  $t=T/T_c$ ,  $b=\hbar H_c D \sigma / 2 \phi_0 k_B T_c$  and  $u(x)=\psi(1/2+x)-\psi(1/2)$ .  $\psi(x)$  is the digamma function,  $D_\sigma$  is the  $\sigma$  band diffusivity,  $\phi_0$ , the flux quantum, and  $\eta$  is the ratio of the  $\pi$  band diffusivity to that of the  $\sigma$  band ( $D_\pi/D_\sigma$ ).  $w$  and  $\lambda_{1,2}$  are related to the electron-phonon coupling constant  $\lambda_{mn}$  and the Coulomb pseudopotential matrix  $\mu_{mn}$ . In this work, interband scattering effects are not considered for simplicity, as the effects of interband scattering can be neglected when the reduction in the transition temperature is relatively small.<sup>15,33-36</sup> The best fit is obtained with diffusivities of 1.2×10<sup>-4</sup>, 2.7×10<sup>-6</sup>, 2.5×10<sup>-4</sup> and 0.65×10<sup>-4</sup> m<sup>2</sup> s<sup>-1</sup> for the doped sample, and 1.6×10<sup>-4</sup>, 4.2×10<sup>-6</sup>, 4.2×10<sup>-4</sup> and 1.1×10<sup>-4</sup> m<sup>2</sup> s<sup>-1</sup> for the un-doped sample, which correspond to  $D_\sigma^{ab}$ ,  $D_\pi^{ab}$ ,  $D_\sigma^c$  and  $D_\pi^c$ , respectively (see also Supplementary Table SI). It is clear that the impurity scattering rate is indeed increased by malic acid doping.

### Microscopic origin for the enhanced high-field properties

To elucidate the microscopic origin of the increase in the impurity scattering rate, which increases the upper critical field and thereby the high-field critical current density, the atomic structure of both the malic acid-doped and the un-doped samples was investigated using a 300 keV field-emission high-resolution transmission electron microscope (TEM). Samples were prepared by a wedge polishing method and then ion milled with a low acceleration voltage of 0.1 keV. A notable difference between samples is that with malic acid doping, many stacking faults were present (red arrows in Figure 3a), whereas it was hard to find any trace of stacking faults in the un-doped sample (see also Supplementary Figure S1). The stacking faults were magnified and filtered for more accurate observation (Figure 3b). An inverse fast Fourier transform was taken for Figure 3b, which proceeded with  $g_{002}$  and  $g_{00\bar{2}}$  patterns. Edge dislocations could be pinpointed, as shown in Figure 3c. The Burgers vector of these dislocations was found out to be  $\frac{1}{2}[001]$ . Even dislocation climbs were observed, for example, as is indicated with a yellow circle in Figure 3b. Dislocation climbs in hexagonal close-packed structure have been reported previously,<sup>37</sup> but not for MgB<sub>2</sub>. Dislocation climbs occur by the diffusion-assisted movement of atomic vacancies and generate intrinsic stacking faults, where a plane is missing from the original crystal structure. To see vacancies clearly, the dislocation climb was magnified further using annular dark-field scanning TEM (ADF-STEM), as shown in Figure 3d, where the stacking faults are marked with white arrows. The lattice orientation is indicated in Figure 3d, and individual magnesium and boron layers can be identified. From a comparison of the ADF-STEM image intensity with electron energy loss spectrum analysis (EELS), it was found that the bright spots correspond to magnesium atoms and the less bright ones to boron atoms (see also Supplementary Figure S1). However, along the stacking faults, boron spots cannot be found, suggesting that a boron layer is missing. Across the stacking faults, along area 1 and area 2, marked with white boxes in Figure 3d, ADF-STEM intensity scans were carried out, as shown in Figure 3e, which clearly indicates that vacancies arise from boron deficiency.

These boron vacancies generate lattice distortion. High-energy synchrotron radiation X-ray powder diffraction using a large Debye-Scherrer camera was conducted at SPring-8 and was analyzed by Rietveld refinement (see also Supplementary Table SII). The boron deficiency reduces the *a*-axis lattice parameter from 3.0832 (2) to 3.0758 (2) Å, while leaving the *c*-axis lattice parameter more or less the same, from 3.5221 (2) to 3.5237 (2) Å. The refinements also show that the crystallite size, or the grain size, was slightly decreased by malic acid doping from 44 to 40 nm. As already noted, a smaller grain size can increase the pinning force, and the increase in the effective pinning force can be partially attributed to the reduction in the grain size. The lattice distortion obtained from the refinement was almost doubled by doping from 0.34 to 0.63%. The correlation between the lattice disorder, the resistivity and the transition temperature is quite well established.<sup>17</sup> Furthermore, it has recently been argued that the upper critical field is related to the resistivity and the transition temperature.<sup>12</sup> The diffusivities listed in the previous paragraph are decreased by doping, or in other words, the impurity scattering rate is increased (see also Supplementary Table SI). For the almost isotropic  $\pi$  bands originating from the  $p_z$  orbitals of the boron atoms, the reduction is also quite isotropic. The reduction in the diffusivities by doping for the  $\pi$  bands,  $D_\pi^{ab}$  and  $D_\pi^c$ , are 0.64 and 0.59, respectively. On the other hand, for the highly anisotropic  $\sigma$  bands from the in-plane  $p_{xy}$  orbitals, the reduction in diffusivity is not uniform. More severe reduction can be found along the *c* axis.  $D_\sigma^c$  is reduced by doping by a

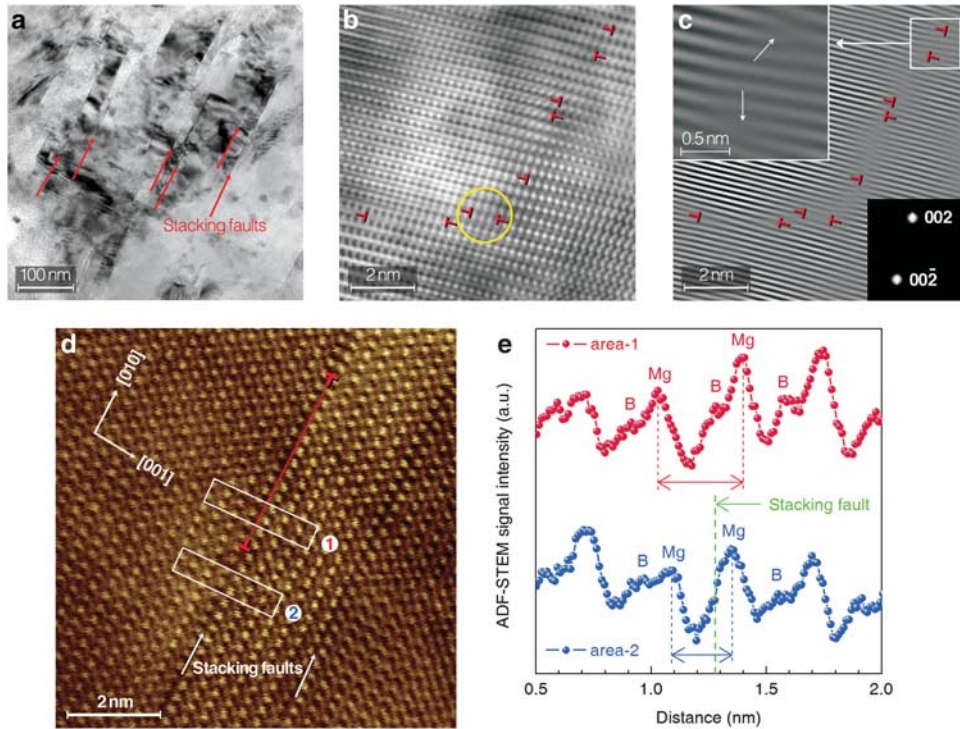


**Figure 3** Microscopic analysis of the core region of the malic acid-doped sample. (a) Low-magnification transmission electron microscope (TEM) image. (b) High-magnification filtered TEM image. Edge dislocations are marked. An intrinsic stacking fault is marked with a yellow circle. (c) The same area as shown in (b) was further image processed using  $g_{002}$  and  $g_{00\bar{2}}$  spots, with the upper inset showing the indicated area at higher magnification and the lower inset the Fast Fourier transform (FFT) pattern. (d) Edge dislocations are marked, and the thick red guideline corresponds to a boron layer. Along the white arrows, boron layers are missing, as can be more clearly seen in (e). (e) Dislocation climb of  $b=\frac{1}{2}[001]$  leading to partial dislocation on the boron layer and stacking faults in the bulk of the MgB<sub>2</sub>.

factor of 0.60, whereas along the  $ab$  plane the reduction in  $D_{\sigma}^{ab}$  is only by a factor of 0.75. We therefore argue that the intrinsic stacking faults caused by boron vacancies are the microscopic origin of the increased impurity scattering rate, which enhances the upper critical field and the other high-field properties.<sup>38</sup>

### The role of carbon for the void reduction

Even though it is generally argued that carbon substitutes for boron, it was not possible to find substituted carbon inside the MgB<sub>2</sub> phase of the malic acid-doped sample, whereas boron vacancies were abundant. A natural question is then where the carbon is. For that purpose, the interface between MgB<sub>2</sub> and impurity phases was further investigated using a Cs-corrected scanning TEM (STEM) equipped with an electron energy loss spectrometer. The majority of the carbon is found to be located outside the MgB<sub>2</sub> phase (region 1 of Figure 4a), mostly at the grain boundaries (region 2), as seen from the detailed EELS analysis shown in Figure 4b. No other peaks were observed other than boron in the EELS for the impurity phase, as shown in Figure 4b. A fast Fourier transform pattern of the impurity phase is featureless, as shown in Figure 4c, reflecting the initial amorphous boron powder. An EELS map for the un-reacted boron phase, where the boron and carbon  $K$  edges are colored blue and red, respectively, is shown in Figure 4d. Thick carbon layers are localized, surrounding a small part of the un-reacted boron, which suggests that the carbon enclosing each boron powder particle during the mixing procedure remains there, even after the reaction heat treatment. The size of the boron particle enclosed by carbon is about 100 nm, which suggests that

carbon suppresses agglomeration of boron, as is schematically depicted in the inset of Figure 4a, leading to denser packing during the metal cladding process and to void fraction reduction. This explains why we do not observe an increase in the low-field critical current density in other carbon-doped samples such as SiC doped.

### CONCLUSIONS

The reaction of magnesium and boron with malic acid has produced critical current densities over a wide field range that are either comparable to or exceed those of commercial NbTi. There is great potential for further enhancement by careful optimization of boron content, while maintaining small grain size. The microscopic origin of the improved high-field properties that is attributed to carbon 'doping' is really due to boron vacancies. Detailed microscopic analysis has shown that boron vacancies generate intrinsic stacking faults within the MgB<sub>2</sub> grains, together with associated lattice distortion. These structural defects produce an increase in the impurity scattering rate, which thereby enhances the upper critical field and the high-field critical current density. Besides enhancing the intragranular scattering via formation of boron vacancies, the inclusion of malic acid leads to boron encapsulation by carbon, which, in turn, prevents agglomeration during heat treatment, yielding fine grains and hence strong pinning. As shown by a detailed void analysis based on X-ray tomography, inclusion of malic acid leads to significant densification (void density decreased from 50 to 40%, and also much finer voids). In short, reaction with malic acid results in a dense, strongly pinned wire core that produces enhanced critical current density, comparable

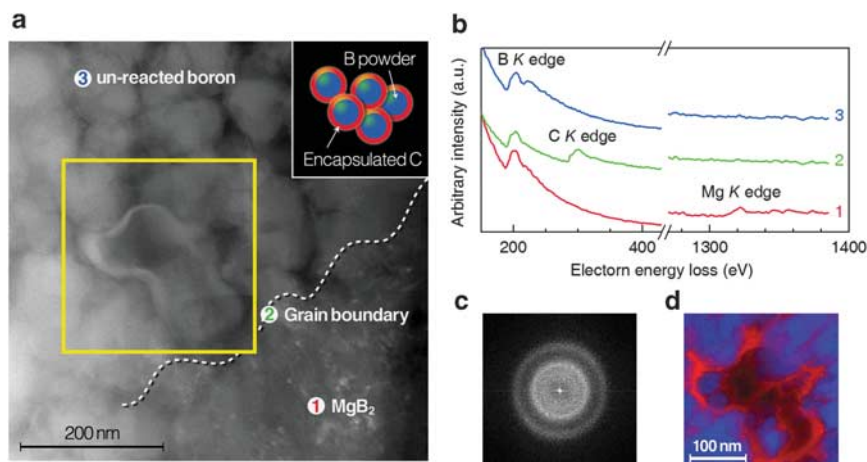


**Figure 4** Microscopic analysis of the grain boundary region of malic acid-doped sample. **(a)** Scanning transmission electron microscope (STEM) image of interface region, with the inset showing a schematic diagram. **(b)** Electron energy loss spectrum (EELS). Carbon *K* peak can be most clearly seen at the interface (region 2). **(c)** Fast Fourier transform (FFT) pattern for the impurity phase. **(d)** Color map of electron energy loss of boron *K* (blue color) and carbon *K* (red color) in a selected area of **(a)** (marked with yellow box).

to that of NbTi in the field range of interest for magnetic resonance imaging.

#### ACKNOWLEDGEMENTS

This work was supported by the Australian Research Council (DP0770205) and Hyper Tech Research Inc., OH, USA. This study was also supported by the Japan Society for the Promotion of Science (JSPS) under the Grant-in-Aid program for JSPS fellows and the Nanotechnology Network Project of the Ministry of Education, Science and Technology (MEST), Japan. The work done at the National Fusion Research Institute was supported by the Mid-career Researcher Program through a National Research Fellowship grant funded by MEST, Japan (no. 2010-0029136). The synchrotron radiation (SR) experiments were performed at the SPring-8 facility with the approval of the Japan Synchrotron Radiation Research Institute (proposal nos. 2008B1557 and 2009A1334). We acknowledge Dr K Ikeda, Professor H Nakashima (Kyushu University, Japan), Dr J Gelb and W Yun (Xradia, Inc., USA) for their support on the XCT measurements. We also thank Dr T Kiyoshi and Dr K Itoh at the National Institute for Materials Science, Japan. We are grateful to Professor K Takase (Nihon University, Japan) and Professor Y Kuroiwa (Hiroshima University, Japan) for their valuable help on the SR experiments at SPring-8; and Dr M Eisterer (Vienna University of Technology, Austria), Professor M Sumpston (The Ohio State University, USA) and Professor XX Xi (Temple University, USA) for their helpful discussions.

**Author contributions:** JHK and SO designed the experiment. Y-UH acquired the TEM experimental data, and JHK, SO and Y-UH wrote the manuscript. The XCT measurements were performed by YS, MM and SH. The XRD experiment at SPring-8 was performed by MM and AM, and SC estimated the wire properties. HK, JLM-D and SXD contributed to the interpretation of the mechanisms.

- Nagamatsu, J., Nakagawa, N., Muranaka, T., Zenitani, Y. & Akimitsu, J. Superconductivity at 39K in magnesium diboride. *Nature* **410**, 63–64 (2001).
- Canfield, P. C., Finnemore, D. K., Bud'ko, S. L., Ostenson, J. E., Lapertot, G., Cunningham, C. E. & Petrovic, C. Superconductivity in dense MgB<sub>2</sub> wires. *Phys. Rev. Lett.* **86**, 2423–2426 (2001).
- Glowacki, B. A., Majoros, M., Vickers, M., Evetts, J. E., Shi, Y. & McDougall, I. Superconductivity of powder-in-tube MgB<sub>2</sub> wires. *Supercond. Sci. Technol.* **14**, 193–199 (2001).
- Larbalestier, D., Gurevich, A., Feldmann, D. M. & Polyanski, A. High-T<sub>c</sub> superconducting materials for electric power applications. *Nature* **414**, 368–377 (2001).

- Ma, Y., Zhang, X., Nishijima, G., Watanabe, K., Awaji, S. & Bai, X. Significantly enhanced critical current densities in MgB<sub>2</sub> tapes made by a scaleable nanocarbon addition route. *Appl. Phys. Lett.* **88**, 072502 (2006).
- Hermann, M., Haessler, W., Rodig, C., Gruner, W., Holzapfel, B. & Schultz, L. Touching the properties of NbTi by carbon doped tapes with mechanically alloyed MgB<sub>2</sub>. *Appl. Phys. Lett.* **91**, 082507 (2007).
- Rowell, M. The widely variable resistivity of MgB<sub>2</sub> samples. *Supercond. Sci. Technol.* **16**, R17–R27 (2003).
- Yamamoto, A., Shimoyama, J., Kishio, K. & Matsushita, T. Limiting factors of normal-state conductivity in superconducting MgB<sub>2</sub>: an application of mean-field theory for a site percolation problem. *Supercond. Sci. Technol.* **20**, 658–666 (2007).
- Wilke, R. H. T., Bud'ko, S. L., Canfield, P. C., Finnemore, D. K., Suplinskas, R. J. & Hannahs, S. T. Systematic effects of carbon doping on the superconducting properties of Mg(B<sub>1-x</sub>C<sub>x</sub>)<sub>2</sub>. *Phys. Rev. Lett.* **92**, 217003 (2004).
- Kazakov, S. M., Puzniak, R., Rogacki, K., Mironov, A. V., Zhigadlo, N. D., Jun, J., Soltmann, C., Batlogg, B. & Karpinski, J. Carbon substitution in MgB<sub>2</sub> single crystal: structural and superconducting properties. *Phys. Rev. B* **71**, 024533 (2005).
- Kortus, J., Dolgov, O. V., Kremer, R. K. & Golubov, A. A. Band filling and interband scattering effects in MgB<sub>2</sub>: carbon versus aluminum doping. *Phys. Rev. Lett.* **94**, 027002 (2005).
- Eisterer, M. Magnetic properties and critical currents of MgB<sub>2</sub>. *Supercond. Sci. Technol.* **20**, R47–R73 (2007).
- Xi, X. X. Two-band superconductor magnesium diboride. *Rep. Prog. Phys.* **71**, 116501 (2008).
- Choi, H. J., Roundy, D., Sun, H., Cohen, M. L. & Louie, S. G. The origin of the anomalous superconducting properties of MgB<sub>2</sub>. *Nature* **418**, 758–760 (2002).
- Gurevich, A. Enhancement of the upper critical field by nonmagnetic impurities in dirty two-gap superconductors. *Phys. Rev. B* **67**, 184515 (2003).
- Gurevich, A., Patnaik, S., Braccini, V., Kim, K. H., Mielke, C., Song, X., Cooley, L. D., Bu, S. D., Kim, D. M., Choi, J. H., Belenky, L. J., Gléncke, J., Lee, M. K., Tian, W., Pan, X. Q., Siri, A., Hellstrom, E. E., Eom, C. B. & Larbalestier, D. C. Very high upper critical fields in MgB<sub>2</sub> produced by selective tuning of impurity scattering. *Supercond. Sci. Technol.* **17**, 278–286 (2004).
- Kim, J. H., Dou, S. X., Oh, S., Jercinovic, M., Babic, E., Nakane, T. & Kumakura, H. Correlation between doping induced disorder and superconducting properties in carbohydrate doped MgB<sub>2</sub>. *J. Appl. Phys.* **104**, 063911 (2008).
- Kim, J. H., Zhou, S., Hossain, M. S. A., Pan, A. V. & Dou, S. X. Carbohydrate doping to enhance electromagnetic properties of MgB<sub>2</sub> superconductors. *Appl. Phys. Lett.* **89**, 142505 (2006).
- Larbalestier, D. C., Cooley, L. D., Rikel, M. O., Polyanski, A. A., Jiang, J., Patnaik, S., Cai, X. Y., Feldmann, D. M., Gurevich, A., Squitieri, A. A., Naus, M. T., Eom, C. B., Hellstrom, E. E., Cava, R. J., Regan, K. A., Rogado, N., Hayward, M. A., He, T., Slusky, J. S., Khalifah, P., Inumaru, K. & Haas, M. Strongly linked current flow in polycrystalline forms of the superconductor MgB<sub>2</sub>. *Nature* **410**, 186–189 (2001).
- Eom, C. B., Lee, M. K., Choi, J. H., Belenky, L. J., Song, X., Cooley, L. D., Naus, M. T., Patnaik, S., Jiang, J., Rikel, M., Polyanski, A., Gurevich, A., Cai, X. Y., Bu, S. D., Babcock, S. E., Hellstrom, E. E., Larbalestier, D. C., Rogado, N., Regan, K. A., Hayward, M. A., He, T., Slusky, J. S., Inumaru, K., Haas, M. K. & Cava, R. J. High critical current density and enhanced irreversibility field in superconducting MgB<sub>2</sub> thin films. *Nature* **411**, 558–560 (2001).
- Martinez, E., Mikheenko, P., Martinez-Lopez, M., Millan, A., Bevan, A. & Abell, J. S. Flux pinning force in bulk MgB<sub>2</sub> with variable grain size. *Phys. Rev. B* **75**, 134515 (2007).



- 22 Mikheenko, P., Martinez, E., Bevan, A., Abell, J. S. & MacManus-Driscoll, J. L. Grain boundaries and pinning in bulk MgB<sub>2</sub>. *Supercond. Sci. Technol.* **20**, S264–S270 (2007).
- 23 Flukiger, R., Suo, H. L., Musolino, N., Beneduce, C., Toulemonde, P. & Lezza, P. Superconducting properties of MgB<sub>2</sub> tapes and wires. *Physica C* **385**, 286–305 (2003).
- 24 Gumbel, A., Eckert, J., Fuchs, G., Nenkov, K., Muller, K. H. & Schultz, L. Improved superconducting properties in nanocrystalline bulk MgB<sub>2</sub>. *Appl. Phys. Lett.* **80**, 2725–2727 (2002).
- 25 Fang, H., Padmanabhan, S., Zhou, Y. X. & Salama, K. High critical current density in iron-clad MgB<sub>2</sub> tapes. *Appl. Phys. Lett.* **82**, 4113–4115 (2003).
- 26 Kumakura, H., Kitaguchi, H., Matsumoto, A. & Hatakeyama, H. Upper critical fields of powder-in-tube-processed MgB<sub>2</sub>/Fe tape conductors. *Appl. Phys. Lett.* **84**, 3669–3671 (2004).
- 27 Sumption, M. D., Bhatia, M., Rindfleisch, M., Tomsic, M., Soltanian, S., Dou, S. X. & Collings, E. W. Large upper critical field and irreversibility field in MgB<sub>2</sub> wires with SiC additions. *Appl. Phys. Lett.* **86**, 092507 (2005).
- 28 Dou, S. X., Shcherbakova, O., Yoeh, W. K., Kim, J. H., Soltanian, S., Wang, X. L., Senatore, C., Flukiger, R., Dhalle, M., Husnjak, O. & Babic, E. Mechanism of enhancement in electromagnetic properties of MgB<sub>2</sub> by nano SiC doping. *Phys. Rev. Lett.* **98**, 097002 (2007).
- 29 Oh, S., Kim, J. H., Cho, K., Lee, C., Kim, C. J., Dou, S. X., Rindfleisch, M., Tomsic, M. & Ahn, J. H. A comparative study on field, temperature, and strain dependences of the critical current for doped and undoped MgB<sub>2</sub> wires based on the percolation model. *J. Appl. Phys.* **106**, 063912 (2009).
- 30 Bugoslavsky, Y., Perkins, G. K., Qi, X., Cohen, L. F. & Caplin, A. D. Vortex dynamics in superconducting MgB<sub>2</sub> and prospects for applications. *Nature* **410**, 563–565 (2001).
- 31 Komori, K., Kawagishi, K., Takano, Y., Fujii, H., Arisawa, S., Kumakura, H., Fukutomi, M. & Togano, K. Approach for the fabrication of MgB<sub>2</sub> superconducting tape with large in-field transport critical current density. *Appl. Phys. Lett.* **81**, 1047–1049 (2002).
- 32 Eisterer, M., Zehetmayer, M. & Weber, H. W. Current percolation and anisotropy in polycrystalline MgB<sub>2</sub>. *Phys. Rev. Lett.* **90**, 247002 (2003).
- 33 Erwin, S. C. & Mazin, I. I. Toward one-band superconductivity in MgB<sub>2</sub>. *Phys. Rev. B* **68**, 132505 (2003).
- 34 Gonnelli, R. S., Daghero, D., Calzolari, A., Umrinario, G. A., Dellarocca, V., Stepanov, V. A., Kazakov, S. M., Zhigadlo, N. & Karpinski, J. Evidence for single-gap superconductivity in Mg(B<sub>1-x</sub>C<sub>x</sub>)<sub>2</sub> single crystals with  $x = 0.132$  from point-contact spectroscopy. *Phys. Rev. B* **71**, 060503 (2005).
- 35 Tsuda, S., Yokoya, T., Kiss, T., Shimojima, T., Shin, S., Togashi, T., Watanabe, S., Zhang, C., Chen, C. T., Lee, S., Uchiyama, H., Tajima, S., Nakai, N. & Machida, K. Carbon-substitution dependent multiple superconducting gap of MgB<sub>2</sub>: a sub-meV resolution photoemission study. *Phys. Rev. B* **72**, 064527 (2005).
- 36 Szabo, P., Samuely, P., Pribulova, Z., Angst, M., Bud'ko, S., Canfield, P. C. & Marcus, J. Point-contact spectroscopy of Al- and C-doped MgB<sub>2</sub>: superconducting energy gaps and scattering studies. *Phys. Rev. B* **75**, 144507 (2007).
- 37 Heo, Y. U., Takeguchi, M., Furuya, K. & Lee, H. C. Transformation of DO<sub>24</sub> η-Ni<sub>3</sub>Ti phase to face-centered cubic austenite during isothermal aging of an Fe-Ni-Ti alloy. *Acta Materialia* **57**, 1176–1187 (2009).
- 38 MacManus-Driscoll, J. L., Zerrer, P., Wang, H. Y., Yang, H., Yoon, J., Fouchet, A., Yu, R., Blamire, M. G. & Jia, Q. X. Strain control and spontaneous phase ordering in vertical nanocomposite heteroepitaxial thin film. *Nat. Mater.* **7**, 314–320 (2008).



This work is licensed under the Creative Commons Attribution-NonCommercial-Share Alike 3.0 Unported License. To view a copy of this license, visit <http://creativecommons.org/licenses/by-nc-sa/3.0/>

Supplementary Information accompanies the paper on the NPG Asia Materials website (<http://www.nature.com/am>)